Shao et al. *Microsystems & Nanoengineering* (2026)12:183
https://doi.org/10.1038/s41378-026-01310-4

Microsystems & Nanoengineering
www.nature.com/micronano

ARTICLE Open Access

A high-throughput modular microfluidic platform for versatile functional assays at single-cell level

Ning Shao[1]✉, Junhua Mai[1], Biana Godin[1] and Xuewu Liu[1]✉

Abstract

Understanding how individual cells behave is essential for uncovering the complexity of biology and disease, yet most single-cell technologies provide only static molecular snapshots. We present the High-throughput Single-Cell Omni-functional Profiling Engine (HiSCOPE), a microfluidic platform that directly investigates functional dynamics of ≥10,000 single cells. HiSCOPE integrates a hydrodynamic single-cell trapping array with customized modular assay chambers to reproducibly trap single cells, pairs, and trios of cells originating from distinct populations and to support diverse functional assays—including viability, proliferation, cytotoxicity, cytokine secretion, and contact-dependent and -independent cell–cell interactions. Importantly, live-cell retrieval enables downstream analysis of selected cells. We demonstrate HiSCOPE's utility by evaluating leukemia cells' drug susceptibility, profiling natural killer (NK) cell cytotoxicity and cytokine secretion, and dissecting T cell–macrophage crosstalk. Our results reveal striking functional diversity that is masked in bulk assays. HiSCOPE offers a scalable solution for functional profiling of single cells, with broad implications for biology, immunotherapy, and personalized medicine.

Introduction

Cellular heterogeneity is a fundamental hallmark of biological systems. Single-cell analysis has revolutionized our understanding of this heterogeneity, leading to remarkable discoveries across cancer biology, immunology, developmental biology, and drug development. The advent of high-throughput single-cell omics technologies has enabled molecular characterization of single cells at unprecedented scale and depth, revealing cellular compositions, rare subpopulations, dynamic cellular states, and lineage trajectories that are masked in bulk assays[1]. Despite these remarkable advances, a critical gap remains. Although molecular signatures can often be linked to cellular functions and behaviors, such indirect indicators are frequently inaccurate due to complex regulatory mechanisms and therefore do not fully reflect dynamic cellular functions[2,3]. As a result, secondary screens or bulk assays are typically required to more reliably determine how cells respond to therapeutics or stimuli, or interact with other cells. Direct measurement of dynamic functional behaviors of single cells, such as cell viability, proliferation, cytotoxicity, secretion, and cell–cell interactions, provides important information that complements molecular profiling. This leads to a deeper and more comprehensive understanding of underlying biological processes and supports more reliable development and personalization of novel therapies.

Microfluidics has the potential to fill this gap owing to its capability to isolate, manipulate, and analyze single cells with precise control and high throughput[4,5]. For example, valve-based microfluidic systems[6,7], hydrodynamic trap arrays[8–13], high-density microwell/microchamber arrays[14–19], and droplet-based systems[20–23] now permit analysis of cell proliferation, secretion, and cell–cell interactions of hundreds to hundreds of thousands of single cells in parallel. Despite their rapid development and promising potential, existing microfluidic single-cell platforms still face method-specific and fundamental limitations that hinder comprehensive functional analysis. Valve-based microfluidic systems provide precise temporal control of the microenvironment but typically scale to only tens to hundreds of chambers due to the complexity of pneumatic routing and

Correspondence: Ning Shao (shaoning064@gmail.com) or Xuewu Liu (xliu@houstonmethodist.org)
[1]Center for BioNanoengineering, Houston Methodist Research Institute, Houston, TX, USA

multilayer fabrication, limiting their applicability for large-scale single-cell functional screening[6,24]. Hydrodynamic trap arrays enable deterministic single-cell capture and relatively high throughput; however, trapped cells are commonly exposed to shear stress due to continuous perfusion during trapping and culture, which also removes autocrine and paracrine factors, potentially altering cellular states and limiting studies of shear-sensitive or autocrine/paracrine-dependent behaviors[8,25]. Microwell and microchamber arrays offer high-density layouts for secretion profiling or short-term cell–cell interaction studies; however, stochastic Poisson-limited loading results in low single-cell occupancy, wasting a large fraction of assay units[17]. In addition, closed-format wells suffer from restricted nutrient and waste exchange, making them unsuitable for long-term proliferation or drug-response assays, whereas open-format wells sacrifice precise control of the cellular microenvironment[15,16]. Droplet-based microfluidic systems achieve ultrahigh throughput but encapsulate cells in isolated aqueous droplets surrounded by oil, which severely limits sustained culture, cell adhesion, migration and controlled cell–cell interactions, in addition to Poisson-limited low single-cell occupancy[21–23]. Electrical, optical, acoustic, and magnetic methods have also been integrated with microfluidics for single-cell manipulation and analysis but are more complicated and typically require additional instrumentation or specialized setups[26,27]. Importantly, most existing platforms are function-specific, designed to interrogate only one or two cellular behaviors, such as proliferation, cytotoxicity, or secretion, rather than enabling integrated, multimodal functional profiling. Moreover, the lack of reliable and selective live-cell retrieval in closed microfluidic formats prevents direct linkage between dynamic functional phenotypes and downstream molecular characterization[10]. Together, these limitations underscore the unmet need for a single-cell functional analysis platform that combines deterministic loading, high throughput, shear-free long-term culture, modular assay geometries, and selective live-cell retrieval within a single integrated system.

To overcome these limitations, we developed the High-throughput Single-Cell Omni-functional Profiling Engine (HiSCOPE), a modular microfluidic platform designed for large-scale, multimodal single-cell functional analysis. HiSCOPE integrates deterministic single-cell and cell-pair loading with centrifugation-directed homing into dead-end, no-flow assay chambers, enabling shear-free long-term culture and spatially programmable cell–cell configurations within a unified trapping array. Importantly, the decoupled modular design allows diverse functional assays to be implemented without redesigning the core trapping architecture, while supporting 12,800 parallel assay units per chip and selective retrieval of single cells of interest after on-chip interrogation for downstream clonal expansion or molecular profiling. This combination of deterministic loading, shear-free long-term culture, modular assay flexibility, and live-cell retrieval is, to our knowledge, not simultaneously available on existing single-cell microfluidic platforms. Using this platform, we demonstrate high-throughput single-cell proliferation and drug susceptibility profiling, integrated analysis of immune-cell cytotoxicity and cytokine secretion, and spatially controlled dissection of contact-dependent and paracrine cell–cell interactions. Together, these results establish HiSCOPE as a versatile toolbox for systematically interrogating functional heterogeneity at the single-cell level.

Results

Principle, operation and performance of the high-throughput single-cell loading

The HiSCOPE toolbox includes a series of microfluidic chips designed using AutoCAD and fabricated by standard soft lithography and polydimethylsiloxane (PDMS) molding techniques. A typical microfluidic chip is composed of 64 parallel channels for cell loading, each containing 200 single-cell traps and functional chambers adjacent to each trap for single-cell assays, reaching a total of 12,800 single-cell assay units (Fig. 1a and Figs. S1–2). The embedded row and column numbers help to locate, record, and analyze cells of interest. The single-cell trap has a half-cup structure with an opening the size of cells to be trapped and a short and narrow leakage channel at the bottom (Fig. S2). The half-cup design enables capture and holding of single cells while also allowing their subsequent homing into the adjacent chambers. Efficient cell trapping relies on a combination of three different strategies: (1) the long loop bypass channel significantly increases flow resistance for cells to flow through it; (2) the semicircular cell-focusing structure near the trap helps to focus the cells toward the trap side; (3) temporary cell crowding while passing through the cell-focusing structure forces one of the cells into the fluid flowing through the trap. Once a single cell occupies the trap, it significantly increases the flow resistance, redirecting subsequent cells to downstream traps via the bypass channel (Fig. 1b and Fig. S3a). The dimensions of the features (with a universal height of 20 μm) were carefully tuned to trap and retain single cells with diameters ranging from 7 μm to 20 μm (Fig. S2). The dimensions could be further tuned to obtain optimized results for specific cell types. The flow rate and pressure can be adjusted to allow single cells of different sizes to be trapped in the cell traps. After cell trapping, the whole chip is centrifuged. The centrifugation force drives the trapped cells into the adjacent cell assay chambers simultaneously (Fig. 1a, c).

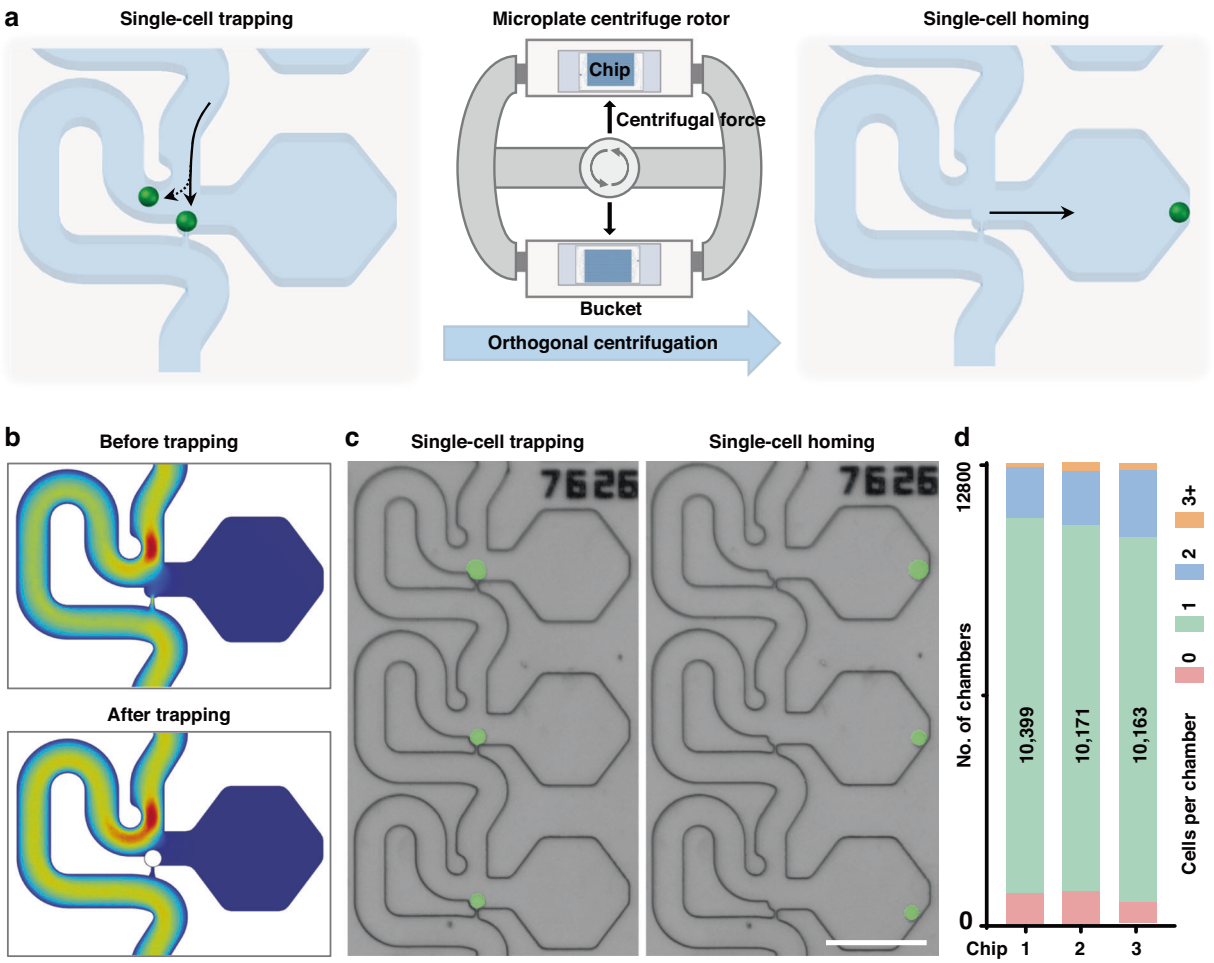

Fig. 1 Principle, operation, and performance of the high-throughput single-cell loading. a Cell loading principle. See details of the centrifugation-enabled single-cell homing in Fig. S4. **b** Flow simulation before and after cell trapping. **c** Representative images of the single-cell trapping and homing. Scale bar, 100 μm. **d** Cell loading results from three chips

Prior to loading cells, the chip is loaded with cell culture medium (optionally with extracellular matrix proteins for adherent cells) and incubated for at least 2 h to prime the chip and reduce nonspecific binding of cells in the channels and traps. The dead-end cell chambers can be filled by either pre-vacuuming the chip or applying a positive pressure to the chip to expel air from the chambers (Fig. S3b). Then, 10–20 μL of the cell suspension at an optimal concentration is added to the inlet reservoir, and a negative pressure is applied at the outlet reservoir to drive the cells into the channels. After filling all the traps with cells, the remaining cells in the inlet, cell-loading channels, and the outlet are washed away with fresh cell culture medium. Then, both the inlet and the outlet reservoirs are filled with fresh medium, with medium level higher in the inlet to avoid reverse flow, and the whole chip is placed in a 50-mL conical tube for centrifugation. A homemade adapter was employed to hold the 50-mL tube horizontally for centrifugation (Fig. S4). Centrifugation at 400–500 × g for 1 min is usually enough to drive the single cells in the traps into the adjacent cell chambers. After cell homing, the chip is ready for various functional assays. Cell loading efficiency was systematically optimized with respect to cell concentration (Fig. S5) and the applied negative pressure (Fig. S6). Higher concentrations (3–6 × 10^6 cells/mL) improved total occupancy but also increased multicell occupancy. Compared with cell concentration, flow pressure had less impact on cell loading efficiency. The optimized cell loading condition was determined as a cell concentration of 2 × 10^6 cells/mL combined with a flow pressure of ~1 psi. Under this cell loading condition, loading of >10,000 single K562 cells per chip was consistently achieved (Fig. 1d).

For functional cell assays, cell viability is a prerequisite. Calcein AM/propidium iodide (PI) staining performed

after cell loading confirmed high cell viability, owing to the rapid and gentle cell trapping and homing process (Fig. S7). Additionally, the lack of flow and disturbance in the single-cell chambers avoids continuous shear stress and sweeping away of autocrine signaling molecules, which are common limitations of flow-through chamber designs that can compromise long-term viability, motility, and other cellular functions during various assays (Video S1). To verify that diffusion alone supports adequate exchange of nutrients, metabolic waste, and assay reagents between the chamber contents and the cell-loading channels in the absence of convective flow, we monitored the diffusion of three fluorescently labeled molecules (389 Da to 150 kDa) using time-lapse fluorescence imaging. The results confirmed that the diffusion reached an equilibrium state rapidly, ensuring efficient molecular exchange and long-term cell culture and functional assays (Fig. S8). Long-term on-chip cell viability and functionality were further verified by a 48-h proliferation assay using K562 cells (Fig. S9).

Development of HiSCOPE chips containing a variety of single-cell functional assay modules

A unique feature of HiSCOPE is the independent modular design of the cell trapping module and the functional assay modules. A variety of functional assay chambers with different configurations can be integrated into the same cell trapping module without interfering with one another. As shown in Fig. 2a and Fig. S10, functional modules were designed to accommodate single cells, closely located cell–cell or cell–bead pairs, distantly located cell pairs, and cell pairs in a transwell format, in which semi-permeable barriers prevent direct cell contact while preserving paracrine communication. Loading of closely located cell–cell and cell–bead pairs can be realized by repeated cell/bead trapping and chip centrifugation at the same angle, enabling the investigation of contact-dependent cell–cell interactions and the capture and detection of cellular contents of single cells. In particular, by adjusting centrifugation angles, loading of distantly located cell pairs and transwell-format cell pairs can be realized in a controlled manner (Fig. S11), providing a unique and precise single-cell tool for studying cell–cell interactions via paracrine signaling. The simulation results confirmed that switching assay modules or homing cells into assay modules does not alter cell trapping fluidics, highlighting the mutual independence between the cell trapping module and the assay modules, that is, the modularity of the platform (Fig. S12). Representative array-level simulations for all the configurations further confirmed uniform flow distribution (Fig. S13). Representative microscopic images of individual modules are shown in Fig. 2b–e and Fig. S14; the chamber volumes are 215 pL for the module shown in Fig. 2b–c, and 230 pL and 235 pL for the modules shown in Fig. 2d–e, respectively.

Loading more than two cells into a single functional assay chamber can also be achieved by repeated loading. For example, trios of cells consisting of a dendritic cell, a T cell (Jurkat), and a B cell (Raji) were sequentially loaded into the same chambers (Fig. S15a–b), enabling recapitulation of the interactions among follicular dendritic cells, T follicular helper cells, and B cells in germinal centers at single-cell resolution[28]. Unlike cell-squeezing-based microfluidic chambers that cannot accommodate rigid objects[8,10,11], our functional assay modules can accommodate not only deformable cells but also rigid objects of similar size, such as functionalized microbeads (Fig. S15c). This enables interactions with single cells, such as capturing/detecting cellular contents from the co-localized single cell, activating/modulating the single cell either through cell binding to the bead or through cell receiving molecules released from the bead. Because the functional assay modules and the cell trapping module are mutually independent, additional assay chamber configurations can be readily integrated with the current cell trapping module for expanded applications.

Selective live-cell retrieval on the HiSCOPE chip

In closed-format microfluidic systems, post-assay cell retrieval for off-chip expansion and/or analysis is often challenging. Our platform allows bulk retrieval of all the cells within individual chambers by reverse centrifugation and flushing. Moreover, we developed a method for selective release and retrieval of single cells of particular interest from the single-cell assay chambers using a micromanipulation setup (Fig. 3a). For this purpose, the chip fabrication process was slightly modified, inspired by the work of Dura et al.[8]. The PDMS device was irreversibly bonded to a thin (~20 μm) PDMS membrane spin-coated on a glass slide. The modified chips could still be used for single-cell functional assays in the same way as unmodified chips. After on-chip assays, because the thin PDMS membrane was reversibly attached to the glass slide, the PDMS device covered by the PDMS membrane could be detached from the glass slide as a whole, then flipped and reattached to a glass slide to expose the thin membrane-covered cell chambers on top while still retaining the cells within their original chambers. The chip was then placed under a microscope equipped with a micromanipulation setup to locate the cells of interest. Because the membrane was thin and elastic, a glass capillary microtip controlled by the micromanipulator was used to extrude the targeted cell into the cell-loading channel by repeatedly pressing the membrane toward the chamber with the microtip. The extruded cell was flushed to the inlet by reverse flow, then retrieved with a standard pipette. To demonstrate the on-chip single-cell retrieval,

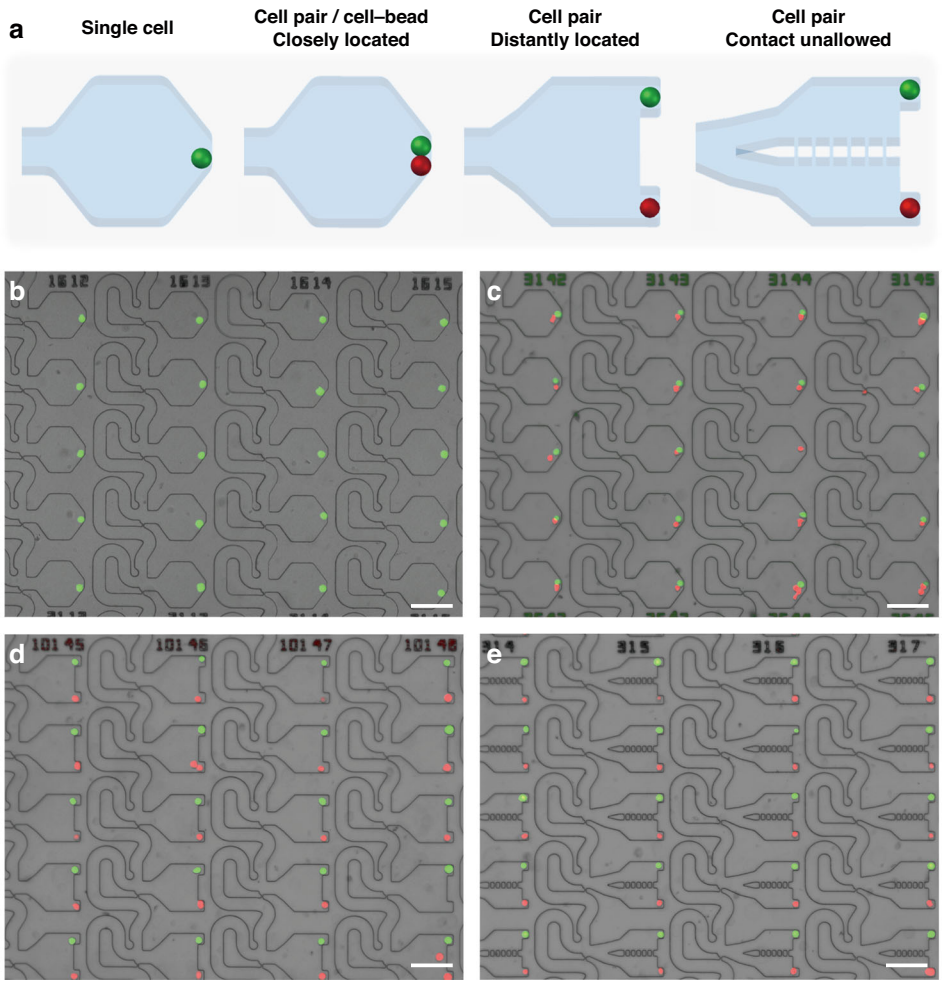

Fig. 2 Design and development of HiSCOPE chips containing single-cell, cell–cell, and cell–bead pair arrays with different functional assay modules. a Designs of different cell/bead-loaded functional assay modules. Images showing the generation of arrays of single cells (**b**), closely located cell–cell pairs (**c**), distantly located cell pairs (**d**), and distantly located cell pairs with direct cell contact prevented (**e**). Scale bars, 100 μm

Calcein AM-labeled K562 cells were loaded to a chip with the aforementioned modifications. After a 2-h resting period, the chip was operated as described above to isolate and retrieve single cells of interest from the chambers (Fig. 3b). As shown in Fig. 3b, extrusion of the desired single cell did not disturb the neighboring cells. The whole cell retrieval procedure takes ~3 min per cell on average, with a retrieval efficiency of ~80% (12 successful retrievals out of 15 attempts in our test). The individual cells were transferred to 96-well plates containing 50% K562 cell-conditioned medium and 50% fresh medium, then cultured for clonal expansion (Fig. 3c). After 7 days, most of the retrieved single cells (11 of 12) form colonies (Fig. 3d), indicating that the retrieval procedure preserved high cell viability. Although not demonstrated here, the retrieved single cells could also be directly processed for single-cell multi-omics analysis. This feature demonstrates a possibility to link the single-cell phenotypes, behaviors, and functions obtained on-chip to their comprehensive molecular signatures obtained off-chip.

Single-cell proliferation and drug susceptibility assay on HiSCOPE chips

Drug resistance remains one of the major challenges in cancer therapy, often arising from tumor heterogeneity and the survival of rare cell subpopulations with intrinsic or adaptive resistance mechanisms[29]. Recent advances in single-cell technologies, such as single-cell genomics and transcriptomics, enable researchers to dissect molecular aspects of the heterogeneity at single-cell resolution. However, genomics and transcriptomics alone cannot accurately predict functional outcomes, such as proliferative capacity under drug stress, especially for subpopulations with adaptive resistance mechanisms. To address this gap, we explored HiSCOPE-based high-throughput single-cell proliferation and drug susceptibility assays.

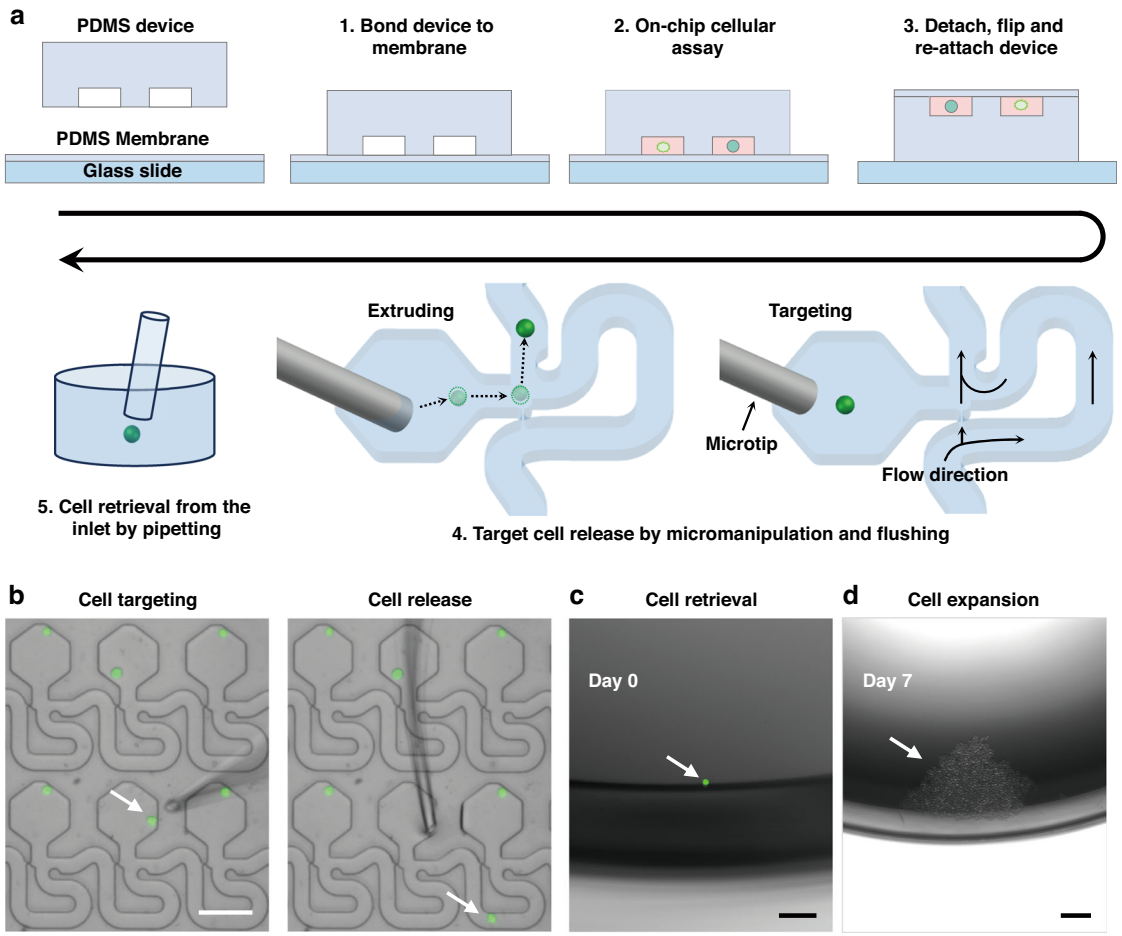

Fig. 3 On-chip live-cell retrieval and off-chip cell expansion. a Schematic illustration of the on-chip selective live-cell retrieval technique. **b** Representative images of single-cell targeting and release. Calcein AM-stained K562 cells were used as an example. The white arrows indicate a single cell targeted and released into the cell-loading channel. **c** A single K562 cell retrieved into a 96-well plate. **d** A cell colony expanded from the single cell shown in (**c**). Scale bars, 100 μm for (**b**) and (**c**), and 200 μm for (**d**)

The human chronic myeloid leukemia (CML) cell line K562 was used as a cancer cell model. Single K562 cell arrays were generated on the chips, each containing more than 10,000 individual K562 cells. After cell loading, the chips were sealed and scanned using a confocal microscope to record cell presence in individual chambers. Cell culture media with DMSO or 2 μM imatinib, an FDA-approved BCR–ABL1 kinase inhibitor for treating CML[30], was continuously perfused through chips in parallel. Every 24 h, the chips were disconnected from the perfusion system and sealed for whole-chip scanning using the confocal microscope. The cells were cultured on-chip for a total of 72 h, followed by staining with PI/Annexin V on-chip to distinguish live, dead, and apoptotic cells. NIS-Elements software (Nikon, Japan) was used to analyze the scanned images and count cell numbers in individual chambers in a semi-automatic manner (Fig. S16a).

As expected, single cells in the control group proliferated significantly, reaching 20–50 cells per chamber within 72 h (Fig. 4a, c). In comparison, imatinib treatment markedly hampered the cell proliferation and viability, resulting in complete cell killing in most chambers after 72 h (Fig. 4b, e). These results are consistent with the cell growth trajectory plot (Fig. S16b) and cell growth rates (Fig. 4d, f). In the control group, the average growth rates were relatively stable over three days (0.96, 0.94, and 0.85 for the first, second and third day, respectively), whereas imatinib caused a dramatic decline (0.82, 0.11, and 0.02, respectively). Data from an additional pair of chips with untreated control or imatinib treatment are shown in Fig. S16c, e. The two replicates show consistent results in cell growth rates (Fig. S16d, f). The three-day single-cell proliferation monitoring combined with subsequent PI/Annexin V staining show that although most cells were killed or undergoing apoptosis after imatinib treatment,

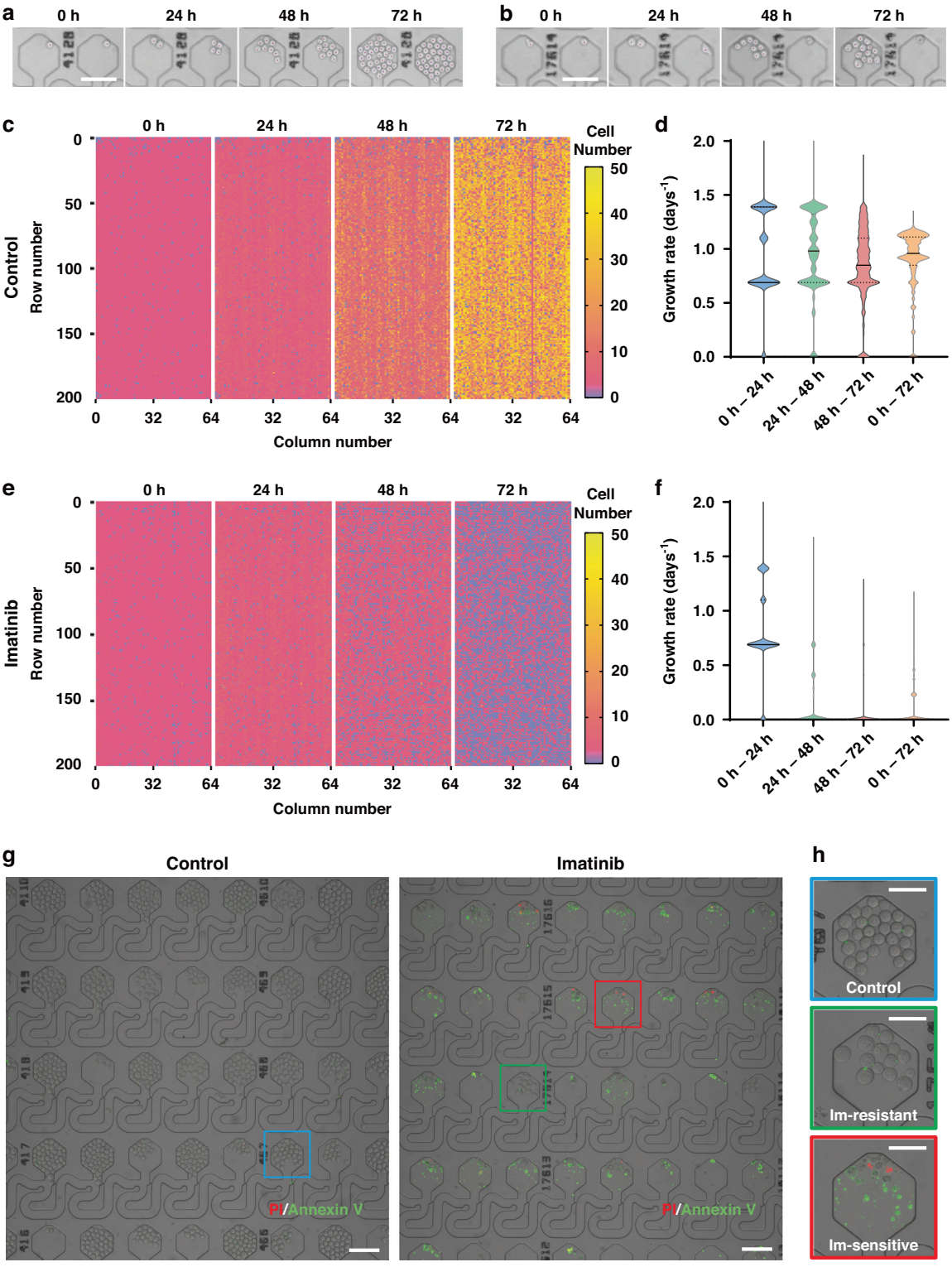

Fig. 4 (See legend on next page.)

(see figure on previous page)

Fig. 4 Single-cell proliferation and drug susceptibility assay on HiSCOPE chips. Human CML cell line K562 was used as a cancer cell model. Images showing cell proliferation in chambers either untreated (**a**) or treated with 2 μM imatinib (**b**) over 72 h. The red dots on each cell are labels automatically marked by the cell-counting software to indicate single cells identified. Heatmaps of cell numbers per chamber for two whole chips either without imatinib treatment (**c**) or treated with 2 μM imatinib (**e**). The heatmap contains 200 rows and 64 columns, with each spot representing a single chamber. The color of each spot represents the number of cells in that chamber. Growth-rate violin plots of the untreated (**d**) and imatinib-treated groups (**f**). Data are from ~20,000 chambers of two independent chips for each group, with each chamber containing a single cell at the beginning of the assay. The black bars represent the median; the dotted lines denote quartiles. **g** On-chip PI/Annexin V staining after 3 days of cell culture. Scale bars, 100 μm. **h** Zoomed-in images of three different chambers showing a healthy single-cell clone without treatment, an imatinib-resistant/-tolerant clone, and an imatinib-sensitive clone individually. Scale bars, 50 μm

there were still a very small subset of single-cell clones that remained proliferating without significant loss of viability, suggesting resistance/tolerance to imatinib (Fig. 4g–h). The variability in cell numbers across chambers under the same microfluidic architecture highlights the intrinsic biological heterogeneity in cell proliferation and drug resistance among the clonally identical cancer cells.

To further investigate the drug resistance/tolerance observed on-chip, we retrieved 102 single-cell-derived clones that remained proliferating with imatinib treatment from 10 chips (Fig. S17a). Twenty clones were individually seeded into a 96-well plate and cultured with imatinib-free medium for 14 days. All the 20 clones were successfully expanded, validating the cell-viability-preserving capability of the on-chip selected retrieval technique (Fig. S17b). The remaining 82 clones were individually retrieved into 96-well plates and cultured with medium containing 2 μM imatinib for 5 days to verify the on-chip drug resistance/tolerance of each clone. Fifty-five clones survived and continued proliferating in the drug-containing medium during the off-chip 5-day imatinib treatment (Fig. S17c). To test whether the observed drug resistance/tolerance was transient, resulting from stress-driven mechanisms such as metabolic rewiring, enhanced efflux, or epigenetic changes, which could be reversible in drug-free culture[29], we rechallenged these 55 surviving clones and the 20 clones cultured in imatinib-free medium with 2 μM imatinib for 3 days following 14 days in drug-free medium (Fig. S17b–c)[31]. Relative cell viability of each clone treated with imatinib normalized to corresponding no-drug controls was evaluated using Cell Counting Kit-8 (CCK-8). Interestingly, most clones (52 of 55) reverted to a fully drug-sensitive state after the 14-day rest in drug-free medium, as indicated by relative viability of <6% upon 3-day imatinib rechallenge, comparable to that of the parental cells. Clones 26, 53, and 64 showed partial imatinib tolerance, maintaining 40.9%, 23.0%, and 17.8% relative viability (Fig. S17d). The half-maximal inhibitory concentration (IC_{50}) of imatinib for parental K562 cells, the clones 26, 53, 64, and three randomly chosen clones lost drug-resistance (clone 5, 39, 60) were then measured using the CCK-8 method (Fig. S17e). Imatinib-resistant/tolerant clones 26, 53, and 64 exhibited significantly higher IC50 values (1.12 μM, 0.68 μM, and 0.67 μM, respectively) than the other three clones and the parental cells (0.11 μM, 0.11 μM, 0.12 μM, and 0.15 μM, respectively), although these values remained lower than those reported for stable imatinib-resistant K562 cells (typically >2 μM)[32]. These data suggest that the drug resistance/tolerance we observed on-chip is mostly transient and reversible drug tolerance induced by acute drug stress, not intrinsic drug resistance due to genomic alterations. These temporarily drug-tolerant clones may be drug-tolerant persisters, which have been found in a variety of cancers, including leukemia, and recognized as one of the major contributors of minimal residual disease (MRD)[29,33]. Collectively, we demonstrated HiSCOPE as a useful tool for evaluating cell proliferation and drug susceptibility at single-cell resolution, as well as identifying and isolating drug-resistant/tolerant clones for mechanistic investigation. This approach could not only improve our understanding of tumor heterogeneity and drug resistance but also guide relapse prediction and combination therapies targeting drug-resistant/tolerant subsets, ultimately improving patient outcomes[33].

Microbead-based single-cell cytokine detection on HiSCOPE chips

Secreted proteins, such as cytokines, growth factors, and antibodies in the surrounding environment are important for trans interactions among cells, regulating immune responses and cell differentiation[19]. Detection of cytokine secretion at the single-cell level provides unprecedented insights into cellular heterogeneity, which could be masked with traditional bulk methods. To this end, we developed an integrated microbead-based single-cell cytokine detection method on HiSCOPE. As shown in Fig. S18a, three different biotinylated cytokine-capture antibodies were co-coated onto streptavidin-conjugated microbeads. Next, single antibody-coated microbeads were co-loaded with individual cells into separate assay chambers to enable capture of cytokines released by adjacent single cells, followed by quantitative measurement via perfusing fluorescently labeled detection antibodies into the chambers. In a proof-of-concept assay, the

beads were coated with antibodies targeting human IL-2, TNF-α, and IFN-γ and calibrated using corresponding recombinant cytokines (Fig. S18b). To validate the on-chip single-cell cytokine detection assay, $CD8^+$ T cells (secretors) spiked with pre-fixed K562 cells (bystanders) were loaded into the chambers at single-cell occupancy, with each chamber containing either a T cell or a K562 cell, followed by loading of the cytokine-capture beads. The cells were stimulated with PMA–ionomycin on-chip and incubated in a cell incubator for 4 h, followed by antibody staining and imaging. An illustration of the step-by-step perfusion procedure is shown in Fig. S19. As expected, stimulated pre-fixed K562 cells showed no detectable cytokine secretion signals, whereas stimulated $CD8^+$ T cells displayed a heterogeneous cytokine secretion profile, confirming the functionality and specificity of the assay (Fig. S18c–d). Among stimulated $CD8^+$ T cells, 28.71% secreted IL-2, 82.67% secreted TNF-α, and 31.68% secreted IFN-γ, while 10.40% secreted all three cytokines.

Integrated single-cell analysis of NK cytotoxicity and cytokine secretion on HiSCOPE chips

The capability of HiSCOPE to pair multiple cells into individual assay chambers in a high-throughput manner enables real-time monitoring of cell–cell interactions at single-cell resolution. To demonstrate this, we paired single NK92MI cells with single K562 cells in the assay chambers and dissected the interaction dynamics between the effectors (NK92MI) and the targets (K562) using 6-h time-lapse imaging. Multiple dynamic interaction patterns were observed (Fig. 5a, Videos S2–S5). Because of excellent controllability and synchrony of the cell pairing, the NK cells and target cells were readily in proximity at the start, without requiring NK cell migration to initiate contact. Owing to the immediate engagement, we were able to observe fast cell killing events occurring within 10 min and delayed killing events occurring after 3–4 h. Moreover, loading multiple effector cells with a single target cell, or vice versa, enabled investigation of combinatorial killing or serial killing by NK cells. We also observed that some NK cells failed to kill target cells regardless of the contact duration. In the absence of paired NK cells, the single K562 cells remained viable throughout the experiments, confirming that the K562 cell death resulted specifically from NK cell-mediated cytolysis. The timing of individual killing events was plotted for different effector-to-target ratios (E/T). Killing times for the $E/T = 1$ and $E/T \geq 2$ groups showed no significant difference, whereas killing times for the $E/T < 1$ group were significantly longer (Fig. 5b). The average killing efficiencies for the $E/T = 1$, $E/T \geq 2$ and $E/T < 1$ groups were 77.1%, 85.3%, and 64.3%, respectively, consistent with the expectation that higher E/T generally results in increased killing efficiency (Fig. 5c). Serial killing is an important feature of NK cell-mediated killing of aberrant cells and may be associated with improved therapeutic outcomes. To investigate serial killing of NK cells in a more controlled manner, single K562 cells were first loaded into each chamber and cultured for 48 h to allow clonal expansion. Single NK cells were then loaded into the chambers, and the cell–cell interactions were monitored by time-lapse imaging for 8 h (Fig. 5d). As shown in Fig. 5e, even when a single NK cell encountered multiple target cells derived from the same cell, which were theoretically equally susceptible, the killing rates varied widely rather than being uniformly 100% (all cells in a chamber were killed, Video S5) or 0% (no cells in a chamber were killed, Video S6). This variability may reflect NK cell exhaustion, heterogeneity in granule release, or subtle differences in contact dynamics during each encounter, warranting further investigation. Interestingly, we found that during the effector cell–target cell interactions, the average migration velocity of the serial killers was significantly higher than that of mono-killers or non-killers (Fig. 5f). This observation links single NK cell migratory behavior with functional outcome and demonstrates the advantage of the HiSCOPE platform in investigating cell–cell interaction dynamics.

To further demonstrate the applicability of HiSCOPE to primary immune cells, we paired primary human NK cells isolated from peripheral blood mononuclear cells (PBMCs) with K562 cells and monitored their interactions (Fig. S20a and Video S7). Killing times for $E/T = 1$ and $E/T \geq 2$ groups again showed no significant difference, whereas killing times for $E/T < 1$ group were significantly longer than those for $E/T \geq 2$ group (Fig. S20b). The average killing efficiencies for the $E/T = 1$, $E/T \geq 2$ and $E/T < 1$ groups were 54.8%, 63.6%, and 34.5%, respectively, consistent with the trends observed in the NK92MI cytotoxicity assays, although overall killing efficiencies were lower (Fig. S20c). Leveraging HiSCOPE's capability of detecting cytokine secretion from single cells, we further evaluated both cytotoxicity and cytokine secretion from individual primary human NK cells (Fig. 5g–i). Statistically, IFN-γ and TNF-α secretion were positively correlated with target cell cytolysis at the population level (Fig. S20d–e). However, single-cell analysis revealed a discordance between cytokine secretion and cytolysis: 25% of NK cells in the $lysis^+$ group failed to secrete IFN-γ or TNF-α, whereas 42.42% of NK cells in the $lysis^-$ group secreted at least one of these cytokines (Fig. 5h). This discordance is in line with previous reports on NK cells and cytotoxic T cells[2,8,17,34], highlighting the necessity of multimodal functional profiling at single-cell resolution for evaluating therapeutic immune cell products.

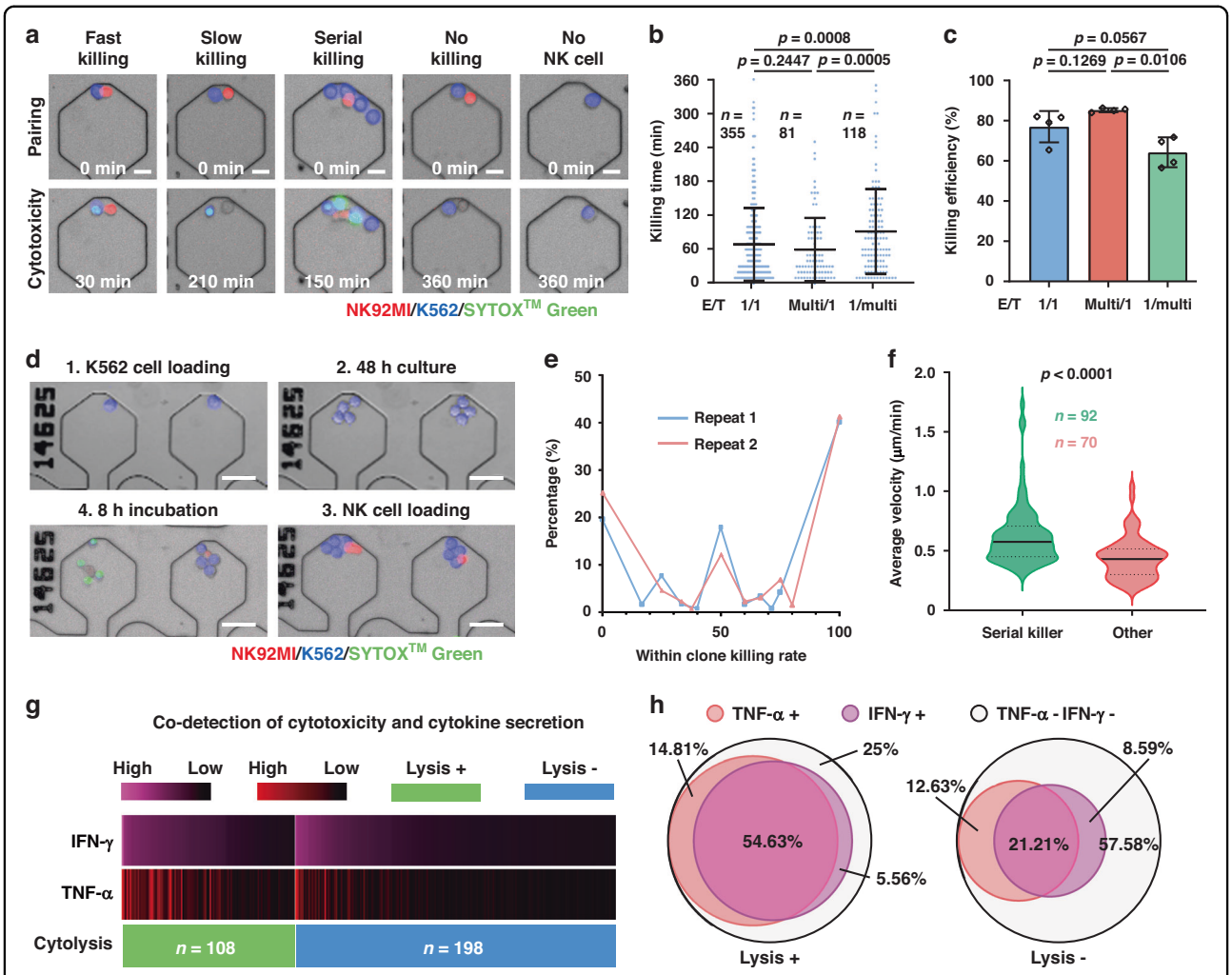

Fig. 5 Integrated single-cell analysis of NK cytotoxicity and cytokine secretion on HiSCOPE chips. a Representative images showing different NK killing patterns. NK92MI cells and K562 cells were stained with Calcein Red-Orange and CellTrace Violet, respectively. Scale bar, 20 μm. **b** Scatterplot of the times of individual killing events at different effector-to-target ratios (E:T). Bars represent mean ± SD. P values were computed using a two-tailed Mann–Whitney test. **c** Killing efficiencies at different E:T. Data represent mean ± SD, n = 4. P values were computed using a two-tailed Welch's *t* test. **d** Representative images showing assay steps of the NK serial killing of single K562 clones. Scale bar, 50 μm. **e** Percentages of different within-clone killing rates (rate = number of killed cells in a clone / total number of cells in the clone) of two independent experiments. **f** Violin plots of the average migration velocities of the serial-killer NK cells and mono-killer/non-killer NK cells. The black bars represent the median, and the dotted lines denote quartiles. P value was computed using a two-tailed Mann–Whitney test. **g** Co-detection of cytotoxicity and cytokine secretion from primary human NK cells. **h** Venn diagrams of TNF-α and IFN-γ secretion in lysis⁺ and lysis⁻ primary human NK cells

Integrated single-cell analysis of T cell–macrophage interactions and cytokine secretion on HiSCOPE chips

Cytokine release syndrome (CRS) and immune effector cell-associated neurotoxicity syndrome (ICANS) are the most frequently observed immune-mediated toxicities in current bispecific T-cell-engaging (BiTE) single-chain antibody constructs and chimeric antigen receptor (CAR) T cell therapies[35]. Growing evidence suggests that interactions between CAR-T cells and macrophages play important roles in these toxicities[36,37]. However, the respective contributions of contact-based and paracrine signaling-based interactions to CRS remain unclear, and investigations of these different interactions along with proinflammatory cytokine secretion at the single-cell level have not been reported. Our unique "single-cell transwell chamber", in which a pair of cells can be positioned on opposite sides (upper and lower compartments) of the chamber, provides a powerful platform to investigate both juxtacrine (cell-contact-mediated) and paracrine signaling-mediated cell–cell interactions at single-cell resolution. To this end, we investigated both contact-mediated and secreted factor-mediated interactions between primary human T cells and macrophages by detecting three well-known proinflammatory cytokines,

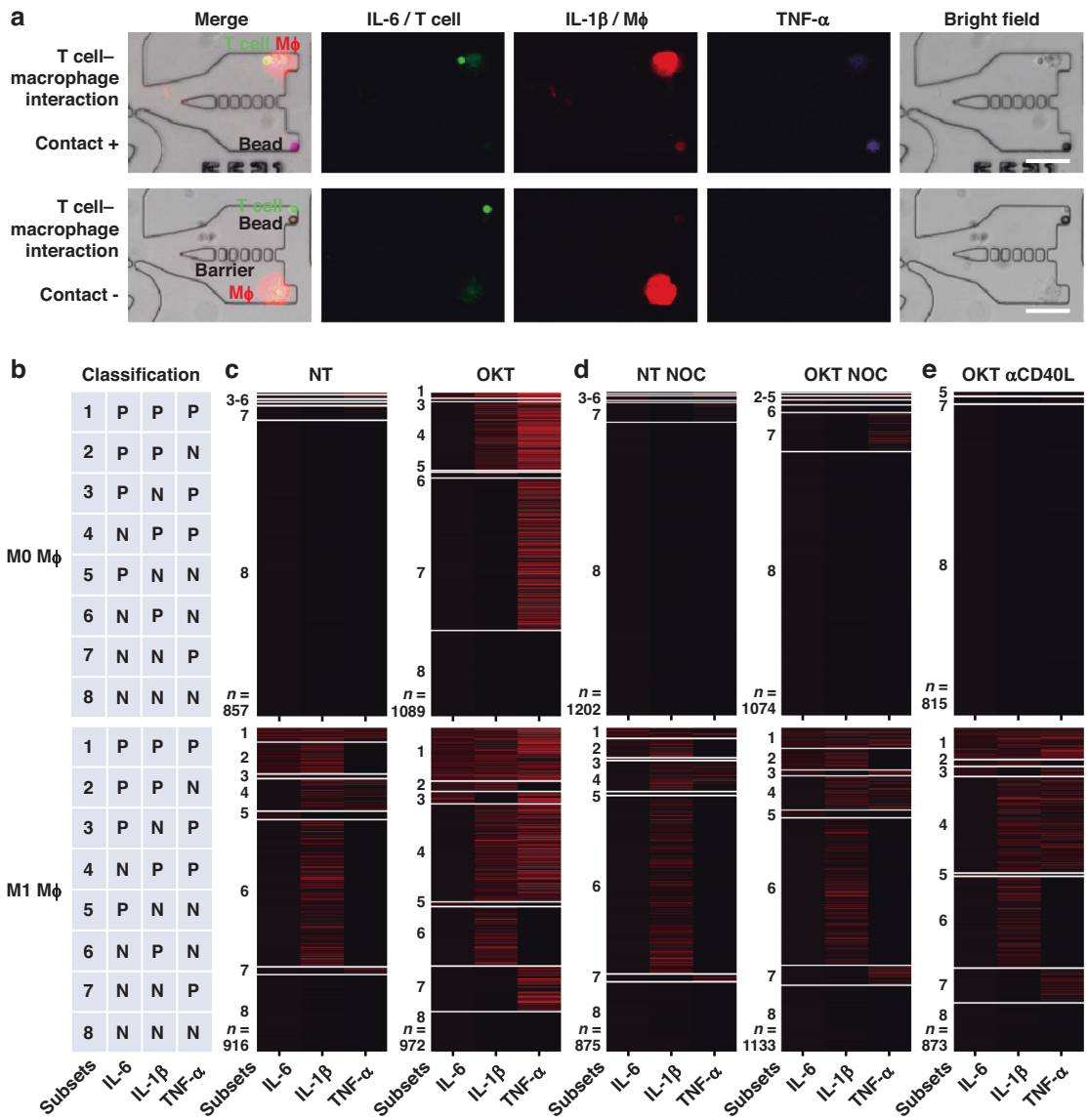

Fig. 6 Integrated single-cell analysis of T cell–macrophage interactions with cytokine secretion on HiSCOPE chips. a Representative images showing the microbead-based cytokine detection from two single human primary T cell–monocyte-derived macrophage (M*ϕ*) pairs either in direct contact or in a transwell format. T cells and macrophages were stained with DiO and DiI, respectively. Scale bars, 50 µm. **b** Functional subset classification based on cytokine secretion profiles. Cytokine secretion heatmaps of different functional subsets under each coculture condition: M0 or M1 macrophages cocultured with nontreated T cells (NT) or 24-h OKT3-treated T cells (OKT), with cell contact (**c**), without cell contact (NOC) (**d**), and with 24-h OKT3-treated T cells with CD40L blocking and cell contact (OKT αCD40L) (**e**). Each row represents a single cell's cytokine profile, and each column indicates a cytokine of interest. The numbers on the left of each heatmap indicate the corresponding functional subsets. Some functional subsets are missing in certain groups because no cells exhibited cytokine secretion profiles falling into these categories. The data are from three independent experiments

namely, IL-6, IL-1β, and TNF-α using the bead-based detection method mentioned above (Fig. S21a). Single T cells and macrophages isolated from the same donor blood samples were paired in cell chambers either in direct contact or in a transwell configuration. Cytokine detection beads were also loaded into the chambers, and the cells were cocultured for 24 h prior to on-chip cytokine detection (Fig. 6a). To prevent crosstalk between adjacent chambers, the chips were perfused with air after cell and bead loading to seal the assay chambers. The sealing remained intact for at least 24 h of incubation (Fig. S21b).

We first examined T cell–macrophage interactions under direct cell-contact conditions. The T cells were

either non-activated or pre-activated with surface-bound OKT3 antibody for 24 h. The M0 macrophages were generated by differentiating blood-derived monocytes using GM-CSF, and M1 macrophages were induced from M0 macrophages by polarizing with LPS and IFN-γ. Single-cell pairs were classified into eight functional subsets based on cytokine secretion profiles (Fig. 6b). We found that coculture of activated T cells with macrophages resulted in significantly increased cytokine secretion compared with non-activated T cell coculture under both M0 and M1 macrophage–T cell conditions. Consequently, functional subset distributions differed markedly between these conditions (Fig. 6c).

Compared with M0 macrophages cocultured with non-activated T cells, coculture with activated T cells increased the proportions of IL-6-, IL-1β-, and TNF-α-secreting cells from 0.70%, 1.40%, and 5.25% to 2.30%, 24.33%, and 71.63%, respectively (Fig. S22a–d). In M1 macrophage cocultures with activated T cells, the percentages of IL-6- and TNF-α-secreting cells increased from 17.03% and 17.03% to 24.07% and 65.23%, respectively. The percentage of IL-1β-secreting cells did not change (70.63% versus 68.93%). To investigate whether the elevation of cytokine secretion in the cocultures was mainly mediated by juxtacrine or paracrine signaling, we paired single T cells and macrophages in the transwell configuration and assessed cytokine secretion after 24 h of coculture. The data indicate that the elevation of cytokine secretion observed in macrophage-activated T cell coculture was predominantly cell-contact-dependent and was strongly reduced under the transwell conditions that prevented direct contact (Fig. 6d). Interestingly, percentages of IL-1β-secreting cells in M1 macrophage–T cell cocultures remained comparable, regardless of direct contact (70.63% and 68.93% in the transwell conditions versus 74.89% and 69.81% in the cell-contact conditions). Taken together with the direct-contact results, these findings suggest that secretion of IL-1β is intrinsic to M1 macrophages and not significantly influenced by T cell coculture.

Binding of CD40 ligand (CD40L), highly expressed on activated T cells, to CD40 on macrophages is known to induce macrophage activation and robust proinflammatory cytokine secretion[38]. We next examined whether blocking the CD40–CD40L interaction between macrophages and T cells using a validated CD40L-neutralizing antibody could suppress the cytokine secretion induced by coculture of macrophages with activated T cells. CD40L blockade almost completely inhibited cytokine secretion in M0 macrophage–OKT3-activated T cell cocultures, whereas its effect on M1 macrophages was less pronounced, suggesting that additional receptor–ligand interactions may contribute to cytokine induction (Fig. 6e). The proportions of functional subsets under each coculture condition were also quantified, revealing substantial functional heterogeneity (Fig. S22e). Collectively, these findings highlight the importance of contact-dependent T cell–macrophage interactions in driving proinflammatory cytokine secretion and reveal pronounced functional heterogeneity and diverse interaction outcomes at the single-cell level, which are not readily captured by existing methods.

Discussion

We have established a versatile platform for high-throughput, multimodal single-cell functional analysis. The half-cup cell trap design, optimized flow resistance, and centrifugation-directed cell homing to the dead-end, shear-free assay chambers enable high cell loading efficiency and minimal perturbation of the cells in the chambers while still allowing for efficient exchange of nutrients, waste and various assay reagents, enabling analysis of >10,000 single live cells and cell pairs per chip in both short-term ($\leq$ 24 h) and long-term assays ($\geq$ 1 week). The centrifugation force for cell homing can be adjusted to different angles, enabling precise manipulation of cell positions in no-flow, dead-end chambers with the coordinated arrangement of various cell chamber layouts. Repeated centrifugation at identical or varying angles further enables positioning of multiple cells at designated locations or sequential relocation of individual cells, thereby expanding single-cell and multicell/bead assay capabilities. The modular design of the cell trapping array and functional assay chamber array allows integration of diverse functional assay chamber modules with the same cell trapping module, providing users with a comprehensive toolbox to perform a variety of common cell functional assays at the single-cell level. By increasing the height of the functional assay chambers, HiSCOPE could also be used for the generation of tumorspheres or organoids, bringing possibilities for cancer stem cell identification, organoid-based high-throughput drug screening and studying organoid-immune cell and organoid-endothelial cell interactions[39,40]. Moreover, it allows for sequential or parallel combination of different functional assays—such as proliferation, cell-surface/intracellular marker staining, cytotoxicity, and secretion profiling—that have been challenging to integrate in a single experiment. In addition, the live-cell retrieval capability provides opportunities to linking cell phenotypes, functions and behaviors with molecular signatures by following single-cell or expanded bulk omics profiling.

Compared with existing microfluidic single-cell platforms, HiSCOPE represents a significant advance in single-cell functional analysis by integrating high throughput, assay modularity, selective live-cell retrieval, and preserved cell viability and intercellular communication enabled by no-flow, shear-free assay chambers

within a single framework—a combination that is not simultaneously addressed by most previously reported systems. For example, a valve-based microfluidic platform has realized multimodal measurements of transcription factor activity, cytokine secretion, and cell movement dynamics from the same single cells; however, it can analyze only ~40 cells in parallel and relies on multilayer fabrication and complex pneumatic valving[6]. Some hydrodynamic trap arrays have enabled deterministic single-cell capture, pairing, and long-term proliferation with relatively high throughput on the order of thousands; however, cells in these systems are continuously exposed to flow-induced shear stress, limiting studies of shear-sensitive or autocrine/paracrine-dependent behaviors, and selective live-cell retrieval has been challenging in these closed-format designs[10,11]. In contrast, another hydrodynamic trap platform that allows selective live-cell retrieval does not support long-term proliferation or preservation of autocrine and paracrine signaling[8]. Microwell and microchamber platforms, such as microengraving and the single-cell barcode chip, enable high-throughput single-cell secretion measurements of 10^3–10^4 individual cells, but generally lack programmable spatial cell–cell configurations or long-term culture environments[14–16]. A droplet platform has characterized CAR T cell-mediated cancer cell killing and cytokine secretion with an ultrahigh throughput exceeding 100,000; however, it does not support programmable spatial cell–cell configurations or continuous monitoring of cell movement dynamics[22]. Together, these comparisons underscore how HiSCOPE fills critical practical gaps between existing platforms, enabling comprehensive functional investigations of single cells within a single system.

While HiSCOPE enables integrated, high-throughput functional interrogation of single cells, several trade-offs of the current implementation warrant discussion. First, the platform requires specific chip-handling steps, such as controlled centrifugation for cell homing, which may introduce operational complexity compared with simpler microwell formats. Although the semi-open, dead-end assay chambers preserve cell viability and autocrine/paracrine signaling, highly motile cells may occasionally migrate out of the chambers during extended assays. Furthermore, although clogging was not observed under the optimized loading conditions used in this study, very high cell concentrations can increase the risk of multi-cell trapping or obstruction of the focusing structures, as with other hydrodynamic focusing systems. Finally, while selective live-cell retrieval is a powerful feature, the current micromanipulation-based implementation is manual and low throughput. Within this design space, HiSCOPE also offers opportunities for further enhancement. For example, platform-specific image-analysis pipelines could be developed to reduce reliance on manual processing and improve overall efficiency, including automated chamber and cell segmentation, cell tracking, fluorescence quantification, and integration of multimodal parameters[10,41]. In addition, physical confinement strategies, such as micropost fences, hydrogels, or selective surface patterning, may further improve retention of highly motile cells during extended assays[42]. Future integration with automated micromanipulation or other high-throughput cell-manipulation methods could substantially improve retrieval throughput[43,44]. Moreover, coupling HiSCOPE with bead-based or spatially patterned barcoding strategies may enable in situ labeling and downstream multi-omics profiling of functionally characterized cells, further strengthening the linkage between dynamic functional phenotypes and underlying molecular mechanisms[45,46]. By enabling researchers to correlate dynamic cellular phenotypes, functions, and behaviors with molecular signatures, HiSCOPE has the potential to advance single-cell biology beyond descriptive molecular profiling and inferential analysis, toward an integrated framework that combines molecular profiling with intuitive, function-based characterization, offering broad applications in cancer research, immunology, and beyond.

Materials and methods

Reagents and materials

Details of the key reagents and materials are summarized in Table S1, unless otherwise described in the following Methods sections.

Cell culture, differentiation, and stimulation

Fresh human PBMCs were purchased from STEMCELL Technologies (Vancouver, BC, Canada). All the subpopulations used in this study, including T cells, NK cells, and monocytes, were isolated using corresponding negative enrichment kits (17951, 19055, and 19359, respectively) from STEMCELL Technologies. The cells were either used immediately after isolation or aliquoted and stored in liquid nitrogen for later use. Human T cells were cultured in RPMI 1640 medium supplemented with 2 mM GlutaMAX, 20 mM HEPES, 10% human AB serum, 1% nonessential amino acids, 1 mM sodium pyruvate, 55 mM β-mercaptoethanol, 100 IU/mL penicillin, 100 μg/mL streptomycin, and 50 IU/mL IL-2 (T-cell medium). Human NK cells were expanded using ImmunoCult NK cell expansion kit (100-0711, STEMCELL Technologies). Expanded NK cells were used immediately after harvest. Human monocytes were cultured in 6-well plates with RPMI 1640 medium supplemented with 2 mM GlutaMAX, 25 mM HEPES, 10% fetal bovine serum (FBS), and 50 ng/mL GM-CSF (Macrophage differentiation medium) for 7 days to differentiate into M0 macrophages. The medium was changed every three days. M0 macrophages

were differentiated to M1 macrophages by adding 100 ng/mL LPS and 20 ng/mL IFN-γ to the medium and culturing for 24 h. Macrophages were used in experiments immediately after harvest. K562 (CCL-243, RRID: CVCL_0004), NK-92MI (CRL-2408, RRID: CVCL_3755), Jurkat (TIB-152, RRID: CVCL_0367), and Raji (CCL-86, RRID: CVCL_0511) cell lines were purchased from the American Type Culture Collection (ATCC, Manassas, VA, USA). K562 cells were maintained in IMDM medium (30-2005, ATCC) with 10% FBS. NK-92MI cells were maintained in MyeloCult H5100 medium (05150, STEMCELL Technologies). Jurkat cells and Raji cells were maintained in RPMI 1640 medium with 10% FBS. All media for the above cell lines were supplemented with 100 IU/mL penicillin and 100 μg/mL streptomycin. All experiments were performed with cells at passages ≤10. Cell cultures were regularly monitored for mycoplasma contamination using the Universal Mycoplasma Detection Kit (30-1012 K, ATCC) and were confirmed to be mycoplasma-free for the described experiments.

Device design, fabrication, and operation

The layouts of the single-cell functional assay chips were designed using AutoCAD software (Autodesk), printed as chrome photomasks (Photo Sciences Inc., Torrance, CA, USA). Flow simulations were conducted using COMSOL Multiphysics v.6.0 (COMSOL Inc., Burlington, MA, USA). A laminar flow model, a flow velocity of 0.01 m/s, and incompressible Navier–Stokes equations were applied. The chips were fabricated using single-layer or double-layer soft photolithography and elastomer molding. Briefly, SU-8 3025 photoresist (MicroChem Corp., Westborough, MA, USA) was spin-coated onto a 4-inch silicon wafer. The structures were 20 μm in height for all applications, except when primary human macrophages were used, in which case the height was modestly increased to 23 μm to better accommodate cell size. The chips with a thickness of 0.5 mm were made by pouring PDMS mixture (10 A: 1B; Sylgard 184 kit, Dow Corning Corp., Midland, MI, USA) over the master mold, degassing and curing at 80 °C for 24 h to fully crosslink the PDMS. The PDMS replica was then peeled off, cut into individual chips, punched, tape-cleaned, treated with oxygen plasma, and bonded to clean, oxygen plasma-treated 3" × 1" glass slides. For the devices compatible with on-chip cell retrieval, only the preparation of the glass slides was modified. PDMS mixture was poured onto clean and non-oxygen plasma-treated 3" × 1" glass slides, spin-coated onto the slides with a speed of 3000 rpm and cured at 80 °C for 30 min. All the devices were sterilized by putting them into a closed metal box and heating at 125 °C for 2 h, then kept in a sterilized environment. All PDMS microfluidic devices were used as disposable consumables to avoid any potential contamination or variability from prior use.

The pre-vacuumed device was primed with the corresponding complete medium for at least 2 h at 37 °C in a cell culture incubator or overnight. To load cells, 10–20 μL of the cell suspension at an optimal concentration (1×10^7 cells/mL for primary T cells and NK cells, and $1–3 \times 10^6$ cells/mL for all the other cells used in this study) was added to the inlet reservoir and perfused by applying a negative pressure (~ 0.2 psi for loading of primary T cells and NK cells, and ~1 psi for loading of other cells) at the outlet reservoir using a tubing-connected syringe mounted on a syringe pump. For larger cell types, increased multi-cell occupancy within individual chambers was observed at cell concentrations of approximately 6×10^6 cells/mL, whereas channel clogging was not observed at this concentration (Fig. S5). For primary T cells and NK cells, increased multi-cell occupancy was observed at concentrations above 2×10^7 cells/mL, and channel clogging was not observed at concentrations up to 1×10^8 cells/mL. When approximately three-quarters of the traps had been occupied, the inlet reservoir was rinsed with medium four times to remove the remaining cells in the inlet and cell-loading channels. When washing started, the remaining cells in the loading channels ensured that the remaining one-quarter of the traps would be occupied. This timing of washing was proven to minimize trapping of multiple cells in a single trap. After washing, the inlet reservoir was filled with fresh medium. The device was carefully disconnected from the tubing, and the outlet reservoir was rinsed with medium to remove all the remaining cells. Then the outlet reservoir was also filled with fresh medium (keeping the medium level lower than the medium level in the inlet to avoid reverse flow). After cell loading, the entire chip was placed in a 50-mL conical tube. The whole tube was placed horizontally in a homemade adapter for centrifugation (Fig. S4) and centrifuged at $400–500 \times g$ for 1 min to drive the single cells in the traps to the adjacent cell chambers. Higher centrifugation speeds ($600–800 \times g$) and shorter time (10–30 s) could be applied to detach cells with high adhesiveness from the traps without damaging the cells. The chip could also be pre-chilled to reduce cell adhesion during trapping if necessary. After centrifugation, the chip was taken out of the tube and put into a 100-mm cell-culture dish. A large PDMS reservoir was assembled on top of the inlet and filled with fresh medium or assay-specific medium. Medium was perfused into the chip by the same negative pumping setup for cell loading, with approximate flow rates between 0.5–1.5 μL/min. The whole dish with the chip inside was incubated in a 37 °C cell culture incubator for the indicated durations, with the left side of the supporting slot raised to produce a ~ 7° tilt, thereby minimizing cell escape.

On-chip cell retrieval

For cell retrieval, the chip fabrication was slightly modified. PDMS devices were plasma-bonded to thin (~20 μm) PDMS membranes that were spin-coated onto glass slides (4000 rpm for 1 min), instead of being directly bonded to glass slides. The slides were cleaned with ethanol and exposed to trimethylchlorosilane (TMCS) vapor for 5 min before PDMS spin-coating to reduce the adhesion between the glass surface and the PDMS membrane, which enabled reliable detachment of the PDMS membrane from glass slides without tearing. The on-chip assay was performed as usual. After the on-chip assay, the PDMS chip covered by the PDMS membrane was detached from the glass slide as a whole, then flipped and reattached to a glass slide. Two sterilized PDMS reservoirs were assembled at the inlet and the outlet. The outlet reservoir was connected to a syringe through tubing. The surface of the PDMS membrane was covered with PBS to minimize evaporation during operation. The entire chip was then placed under a Nikon A1 confocal microscope (Nikon Corporation, Tokyo, Japan) equipped with a micromanipulation setup and examined to locate cells of interest. Before cell targeting, the device was flushed from the outlet with a positive pressure of 1 psi for 3 min to remove any cells that may have occasionally entered the cell-loading channels during chip detaching and flipping. The flushed-out medium was then discarded, and the inlet was washed twice with medium. After cell targeting, a glass capillary microtip (with a 20 μm outer diameter) was controlled by the micromanipulation setup to repeatedly press the membrane at the positions behind the cell toward the chamber to extrude the targeted cell into the cell-loading channel. The single cell or cells from a single clone extruded into the cell-loading channel were then flushed into the inlet with a positive pressure of ~1 psi through the outlet for 1–2 min, depending on the distance between the cells and the inlet. The entire volume of medium in the inlet reservoir was collected into a well of a 96-well plate pre-filled with cell expansion medium (IMDM supplemented with 10% FBS, 100 IU/mL penicillin, 100 μg/mL streptomycin, and optionally 2 μM imatinib) using a standard pipette. The inlet reservoir was washed twice with medium before the next round of retrieval.

Microbeads-based single-cell cytokine detection

Functionalized microbeads for cytokine detection were prepared as previously described[19]. In brief, streptavidin-coated microbeads with a mean diameter of 10 μm (SVP-100-4, Spherotech, Lake Forest, IL, USA) were incubated with 10 μg/mL biotinylated capture antibody cocktail I (anti-IL-2, anti-TNF-α, and anti-IFN-γ) or cocktail II (anti-IL-6, anti-IL-1β, and anti-TNF-α), respectively (Table S1), at room temperature (RT) for 2 h with shaking. The antibody-conjugated microbeads were then incubated with 50 μM biotin to block any unoccupied binding sites, followed by three washes with 1.5% bovine serum albumin (BSA). The beads were resuspended in 1.5% BSA and stored at 4 °C until use. The beads were perfused at a concentration of 3×10^6/mL and loaded into the assay chambers as described above. The cell- and bead-loaded chambers were air-sealed by perfusing air at a high positive pressure (~10 psi) from the outlet. After incubation, the channels and chambers were reconnected by purging air through continuous perfusion with cold medium containing 1.5% BSA into the channels using positive pressure (1–2 psi). After washing away residual cytokines in the chambers, a fluorescently labeled detection antibody cocktail at optimized concentrations was perfused into the chip at 0.5 μL/min for 2 h on ice, optionally followed by incubation at 4 °C overnight. The chip was then washed with cold medium containing 1.5% BSA at 2 μL/min for 2 h at 4 °C. After removal of residual antibodies, the chip was imaged using a Nikon A1 confocal microscope with the "Image Stitch" function.

On-chip NK cytotoxicity assay

NK92MI cells or primary human NK cells were stained with Calcein Red-Orange AM. K562 cells were stained with CellTrace Violet. K562 cells and NK cells were sequentially loaded into the chip. The chip was placed on an EVOS FL Auto microscope (Thermo Fisher Scientific, Waltham, MA, USA) that was housed inside a standard cell culture incubator for time-lapse imaging. During the time-lapse imaging, at least 20 beacons or regions of interest (ROIs) at 10× magnification were recorded per chip at 10-min intervals for a total duration of 6 or 8 h. NK cell medium supplemented with 200 nM SYTOX Green was perfused through the cell-loading channels to indicate dead cells during imaging.

On-chip Macrophage–T cell interaction assay

Macrophages and T cells were stained with DiI and DiO, respectively, then sequentially loaded into the functional assay chambers in the "micro-transwell" format, either in proximity or physically separated. Single cytokine detection beads targeting IL-6, IL-1β, and TNF-α were then loaded into the half chamber that was separated from the macrophages to avoid being phagocytosed during the assay. The chambers were air-sealed and incubated in a 37 °C cell culture incubator for 24 h. Cytokine secretion in each chamber was then detected as described above. To neutralize CD40L on OKT3-activated T cells, T cells were incubated with a validated CD40L antibody (20 μg/mL) for 1 h, then loaded into the chips without removal of unbound antibodies. The subsequent loading and washing media also contained 10 μg/mL of the validated CD40L antibody to ensure adequate CD40L blockade during the coculture.

Image acquisition and analysis

Scanning electron microscopy (SEM) images of the chips were obtained using a FEI Quanta 400 ESEM FEG instrument (Thermo Fisher Scientific). In the single-cell proliferation and drug susceptibility assay, the chips were scanned using the "Image Stitch" function of a Nikon A1 confocal microscope to obtain bright-field images for counting cell numbers in individual chambers. The focus plane was set to make the images slightly blurred to enhance contrast between the cells (brighter) and the background (darker), which facilitated the later cell identification. NIS-Element software was used to count cell numbers in individual cell chambers. A ROI was drawn manually along the edges of the chamber located at the corner of the chip, and ROIs for all other chambers were then efficiently generated by copy-pasting, owing to the regular arrangement of the chambers. Using the "Spot Detection" function with proper spot diameter and contrast settings, the software automatically identified and labeled each single cell in individual chambers, as shown in Fig. S16a. Dead cells, which appeared either darker in the images or fragmented into smaller pieces, were not counted by the software. The cell-number data for individual chambers were exported to Excel files for further analysis. In the NK cytotoxicity assay, time-lapse images of each beacon were stacked and hyperstacked using ImageJ software (National Institutes of Health, Bethesda, MD, USA). Killing of a target cell was indicated by either the presence of green fluorescence on the cell or fragmentation of the cell. Killing times were recorded manually. Cell trajectories were tracked using the "Manual Tracking" plugin in ImageJ. In the single-cell cytokine detection assay, multichannel fluorescence intensities of each bead associated with a single cell were quantified using the "Multi Measure" function in ImageJ. Intensities from chambers without cells were used as the baseline to set thresholds for true-positive secretion.

Statistical analysis

Statistical analyses were performed using GraphPad Prism 8 software (Dotmatics, San Diego, CA, USA). Unpaired Welch's *t*-tests (two-tailed) were used to compare datasets with Gaussian distributions, whereas Mann–Whitney tests were used for datasets without Gaussian distributions. Differences were considered statistically significant when P values were < 0.05. All estimated errors reported for analyses of biological replicates were standard deviation (SD) values, unless otherwise stated in the figure legends.

Acknowledgements
We are grateful for funding support from NIH U01CA244107, NIH R01CA222959, and Houston Methodist Research Institute. We thank the Advanced Cellular & Tissue Microscopy Core of Houston Methodist Research Institute for guidance on image analysis of the single-cell proliferation data. We thank Dr. Jianhua Gu and the Rice University Shared Equipment Authority (SEA) for assistance with SEM imaging of the chips. We thank Dr. Liana Adam for critical reading and editing of the manuscript.

Author contributions
N.S. and X.L. conceived and designed the research. N.S. carried out the experiments and analyzed the data. J.M. and B.J. provided valuable suggestions and resources for the research. All authors contributed to the writing of the manuscript.

Data availability
All data needed to evaluate the conclusions described in this paper are available within the paper and its Supplementary Information. The raw and analyzed datasets are available for research purposes from the corresponding authors upon reasonable request. Source data are provided with this paper.

Competing interests
The authors declare no competing interests.

Supplementary information The online version contains supplementary material available at https://doi.org/10.1038/s41378-026-01310-4.

Received: 21 October 2025 Revised: 19 February 2026 Accepted: 24 March 2026
Published online: 18 May 2026

References

1. Baysoy, A., Bai, Z., Satija, R. & Fan, R. The technological landscape and applications of single-cell multi-omics. *Nat. Rev. Mol. Cell Biol.* **24**, 695–713 (2023).
2. Varadarajan, N. et al. A high-throughput single-cell analysis of human CD8(+) T cell functions reveals discordance for cytokine secretion and cytolysis. *J. Clin. Invest.* **121**, 4322–4331 (2011).
3. Weerakoon, H. et al. Integrative temporal multi-omics reveals uncoupling of transcriptome and proteome during human T cell activation. *NPJ Syst. Biol. Appl.* **10**, 21 (2024).
4. Jammes, F. C. & Maerkl, S. J. How single-cell immunology is benefiting from microfluidic technologies. *Microsyst. Nanoeng.* **6**, 45 (2020).
5. Shao, N. & Qin, L. Biochips—new platforms for cell-based immunological assays. *Small Methods* **2**, 1700254 (2018).
6. Junkin, M. et al. High-content quantification of single-cell immune dynamics. *Cell Rep.* **15**, 411–422 (2016).
7. Prakadan, S. M., Shalek, A. K. & Weitz, D. A. Scaling by shrinking: empowering single-cell 'omics' with microfluidic devices. *Nat. Rev. Genet.* **18**, 345–361 (2017).
8. Dura, B. et al. Longitudinal multiparameter assay of lymphocyte interactions from onset by microfluidic cell pairing and culture. *Proc. Natl. Acad. Sci. USA* **113**, E3599–E3608 (2016).
9. Li, L. et al. A controllable, centrifugal-based hydrodynamic microfluidic chip for cell-pairing and studying long-term communications between single cells. *Anal. Chem.* **91**, 15908–15914 (2019).
10. Yellen, B. B. et al. Massively parallel quantification of phenotypic heterogeneity in single-cell drug responses. *Sci. Adv.* **7**, eabf9840 (2021).
11. Wang, B. et al. An integrated microfluidics platform with high-throughput single-cell cloning array and concentration gradient generator for efficient cancer drug effect screening. *Mil. Med. Res.* **9**, 51 (2022).
12. Gao, Y. et al. An enzyme-loaded metal-organic framework-assisted microfluidic platform enables single-cell metabolite analysis. *Angew. Chem. Int. Ed. Engl.* **62**, e202302000 (2023).
13. Shao, N. et al. A bidirectional single-cell migration and retrieval chip for quantitative study of dendritic cell migration. *Adv. Sci. (Weinh.)* **10**, e2204544 (2023).
14. Shi, Q. et al. Single-cell proteomic chip for profiling intracellular signaling pathways in single tumor cells. *Proc. Natl. Acad. Sci. USA* **109**, 419–424 (2012).
15. Varadarajan, N. et al. Rapid, efficient functional characterization and recovery of HIV-specific human CD8+ T cells using microengraving. *Proc. Natl. Acad. Sci. USA* **109**, 3885–3890 (2012).
16. Lu, Y. et al. Highly multiplexed profiling of single-cell effector functions reveals deep functional heterogeneity in response to pathogenic ligands. *Proc. Natl. Acad. Sci. USA* **112**, E607–E615 (2015).

17. Zhou, Y. et al. Evaluation of single-cell cytokine secretion and cell–cell interactions with a hierarchical loading microwell chip. *Cell Rep.* **31**, 107574 (2020).
18. Li, L. et al. Deciphering cell–cell interactions with integrative single-cell secretion profiling. *Adv. Sci. (Weinh.)* **10**, e2301018 (2023).
19. Shao, N., Zhou, Y. & Liu, X. Multiplexed profiling of single-cell secretion on a hierarchical loading microwell chip. *Biosens. Bioelectron.* **287**, 117711 (2025).
20. Eyer, K. et al. Single-cell deep phenotyping of IgG-secreting cells for high-resolution immune monitoring. *Nat. Biotechnol.* **35**, 977–982 (2017).
21. Matula, K., Rivello, F. & Huck, W. T. S. Single-cell analysis using droplet microfluidics. *Adv. Biosyst.* **4**, e1900188 (2020).
22. Madrigal, J. L. et al. Characterizing cell interactions at scale with made-to-order droplet ensembles (MODEs). *Proc. Natl. Acad. Sci. USA* **119**, e2110867119 (2022).
23. Sart, S., Ronteix, G., Jain, S., Amselem, G. & Baroud, C. N. Cell culture in microfluidic droplets. *Chem. Rev.* **122**, 7061–7096 (2022).
24. Huang, Q., Mao, S., Khan, M. & Lin, J. M. Single-cell assay on microfluidic devices. *Analyst* **144**, 808–823 (2019).
25. Lecault, V. et al. High-throughput analysis of single hematopoietic stem cell proliferation in microfluidic cell culture arrays. *Nat. Methods* **8**, 581–586 (2011).
26. Le, K. et al. A novel mammalian cell line development platform utilizing nanofluidics and optoelectro positioning technology. *Biotechnol. Prog.* **34**, 1438–1446 (2018).
27. Luo, T., Fan, L., Zhu, R. & Sun, D. Microfluidic single-cell manipulation and analysis: methods and applications. *Micromachines (Basel)* **10**, 104 (2019).
28. Vinuesa, C. G., Linterman, M. A., Goodnow, C. C. & Randall, K. L. T cells and follicular dendritic cells in germinal center B-cell formation and selection. *Immunol. Rev.* **237**, 72–89 (2010).
29. Salgia, R. & Kulkarni, P. The genetic/non-genetic duality of drug 'resistance' in cancer. *Trends Cancer* **4**, 110–118 (2018).
30. Savage, D. G. & Antman, K. H. Imatinib mesylate-a new oral targeted therapy. *N. Engl. J. Med.* **346**, 683–693 (2002).
31. Li, M., Wang, X., He, W. & Zhou, H. Drug-tolerant persister cells in acute myeloid leukemia: pressing challenge and promising new strategies for treatment. *Front. Med. (Lausanne)* **12**, 1586552 (2025).
32. Mahon, F. X. et al. Selection and characterization of BCR-ABL positive cell lines with differential sensitivity to the tyrosine kinase inhibitor STI571: diverse mechanisms of resistance. *Blood* **96**, 1070–1079 (2000).
33. Teixeira, A. et al. Current and emerging techniques for diagnosis and MRD detection in AML- a comprehensive narrative review. *Cancers (Basel)* **15**, 1362 (2023).
34. Subedi, N. et al. Single-cell profiling reveals functional heterogeneity and serial killing in human peripheral and ex vivo-generated cd34+ progenitor-derived natural killer cells. *Adv. Biol. (Weinh.)* **7**, e2200207 (2023).
35. Fajgenbaum, D. C. & June, C. H. Cytokine storm. *N. Engl. J. Med.* **383**, 2255–2273 (2020).
36. Morris, E. C., Neelapu, S. S., Giavridis, T. & Sadelain, M. Cytokine release syndrome and associated neurotoxicity in cancer immunotherapy. *Nat. Rev. Immunol.* **22**, 85–96 (2022).
37. Giavridis, T. et al. CAR T cell-induced cytokine release syndrome is mediated by macrophages and abated by IL-1 blockade. *Nat. Med.* **24**, 731–738 (2018).
38. Koguchi, Y., Thauland, T. J., Slifka, M. K. & Parker, D. C. Preformed CD40 ligand exists in secretory lysosomes in effector and memory CD4+ T cells and is quickly expressed on the cell surface in an antigen-specific manner. *Blood* **110**, 2520–2527 (2007).
39. Quintard, C. et al. A microfluidic platform integrating functional vascularized organoids-on-chip. *Nat. Commun.* **15**, 1452 (2024).
40. Lin, D. et al. Screening therapeutic agents specific to breast cancer stem cells using a microfluidic single-cell clone-forming inhibition assay. *Small* **16**, e1901001 (2020).
41. Sun, J., Tarnok, A. & Su, X. Deep learning-based single-cell optical image studies. *Cytom. A* **97**, 226–240 (2020).
42. Li, Y., Motschman, J. D., Kelly, S. T. & Yellen, B. B. Injection molded microfluidics for establishing high-density single cell arrays in an open hydrogel format. *Anal. Chem.* **92**, 2794–2801 (2020).
43. Wu, M. et al. Acoustofluidic separation of cells and particles. *Microsyst. Nanoeng.* **5**, 32 (2019).
44. Zhang, S. et al. Optoelectronic tweezers: a versatile toolbox for nano-/micromanipulation. *Chem. Soc. Rev.* **51**, 9203–9242 (2022).
45. Zhang, M. et al. Highly parallel and efficient single cell mRNA sequencing with paired picoliter chambers. *Nat. Commun.* **11**, 2118 (2020).
46. Chen, T. N., Gupta, A., Zalavadia, M. D. & Streets, A. muCB-seq: microfluidic cell barcoding and sequencing for high-resolution imaging and sequencing of single cells. *Lab Chip* **20**, 3899–3913 (2020).